

version August 13, 2022

CHEERS RESULTS ON MRK 573: STUDY OF DEEP *CHANDRA* OBSERVATIONS

Alessandro Paggi¹, Junfeng Wang¹, Giuseppina Fabbiano¹, Martin Elvis¹ and Margarita Karovska¹

¹*Harvard-Smithsonian Center for Astrophysics, 60 Garden St, Cambridge, MA 02138, USA:*
apaggi@cfa.harvard.edu

ABSTRACT

We present results on Mrk 573 obtained as part of the *Chandra* survey of Extended Emission-line Regions in nearby Seyfert galaxies (CHEERS). This source features a biconical emission in the soft X-ray band, which is closely related with the Narrow Line Region as mapped by the [O III] emission line; we investigate the properties of soft X-ray emission from this source with new deep observations. Making use of the subpixel resolution of the *Chandra*/ACIS image and PSF-deconvolution, we resolve and study substructures in each ionizing cone: the two cone spectra are fitted with photoionization model, showing a mildly photoionized phase diffused over the bicone. A thermal collisional gas at about ~ 1 keV appears to be located near the “knots” resolved in radio observations and between the “arcs” resolved in the optical images, and can be interpreted in terms of shock interaction with the galactic plane. The nuclear region features higher ionization parameter without requiring the presence of thermal gas, and shows a slight flux decrease across the observations together with an increase in the hydrogen column density, indicating variability of the AGN. The long exposure allow us to find extended emission up to ~ 7 kpc from the nucleus along the bicone axis, while significant emission is also detected in the direction perpendicular to the ionizing cones, suggesting the lack of the fully obscuring torus that is prescribed in the AGN unified model, and rather the presence of a clumpy structure not fully covering the line of sight.

Subject headings: galaxies: active - galaxies: individual (Mrk 573) - galaxies: jets - galaxies: Seyfert - X-rays: galaxies

1. INTRODUCTION

The interaction between active galactic nuclei (AGN) and their host galaxy is signaled by the narrow line region and extended narrow line region (NLR, ENLR). This [O III] emitting region, extending on kpc scale and observed in many Seyfert galaxies, is widely interpreted as gas photoionized by the AGN (e.g., [Schmitt et al. 2003](#)).

A key tool to understand this interaction is provided by the study of soft X-ray emission from these sources. The overall structure of the X-ray emission appears to be morphologically correlated with the ENLR, suggesting a common physical origin ([Bianchi et al. 2006](#); [Massaro et al. 2006](#); [Wang et al. 2011c](#)).

In the unified AGN model ([Antonucci 1993](#)) the soft X-ray spectra from Seyfert 2 galaxies are expected to be affected by emission by the circumnuclear medium, illuminated by the nuclear continuum. In fact high resolution spectral and spatial observations, mostly performed with *Chandra* and *XMM-Newton*, have shown that such emission arise from the circumnuclear medium photoionized by the nuclear continuum. In fact, X-ray grating spectroscopy agrees with this picture, showing that the spectra can be interpreted as a blending of emission lines, with little contribution from collisionally ionized plasma (see e.g. [Ogle et al. 2000](#); [Brinkman et al. 2002](#); [Kinkhabwala et al. 2002](#)).

Mrk 573 ($z = 0.017$, [Ruiz et al. 2005](#)) is one of the brightest Seyfert galaxies observed by *HST*, with a ENLR extending to $\sim 9''$ corresponding to a projected size of about 3 kpc¹, where photoionization by the central AGN appears to be the dominant process ([Ferruit et al. 1999](#); [Schlesinger et al. 2009](#)). Mrk 573 is also associated with a triple radio source, with a central core and two side knots ([Ulvestad & Wilson 1984](#)).

The ENLR of Mrk 573 has been modeled by [Fischer et al. \(2010\)](#) making use of *HST* data; the kinematic model developed by these authors features an ionizing bicone with the NW cone tilted toward the observer line of sight, and with a half opening angle of 53° . The observed half opening angle of $\sim 30^\circ$ results from the intersection of the bicone with the galaxy plane. The authors conclude that the circumnuclear emission is mainly due to the intersection of the ionizing bicone with the galactic disk, as supported by the observed emission arcs that coincide with outer dust lanes.

The X-ray emission from Mrk 573 has been previously studied by several authors. A study of EPIC/*XMM-Newton* data by [Guainazzi et al. \(2005\)](#) showed for this source a strong Fe K α

¹In the following, we adopt the standard flat cosmology with $\Omega_\Lambda = 0.73$ and $H_0 = 70 \text{ km s}^{-1} \text{ Mpc}^{-1}$ ([Komatsu et al. 2011](#)).

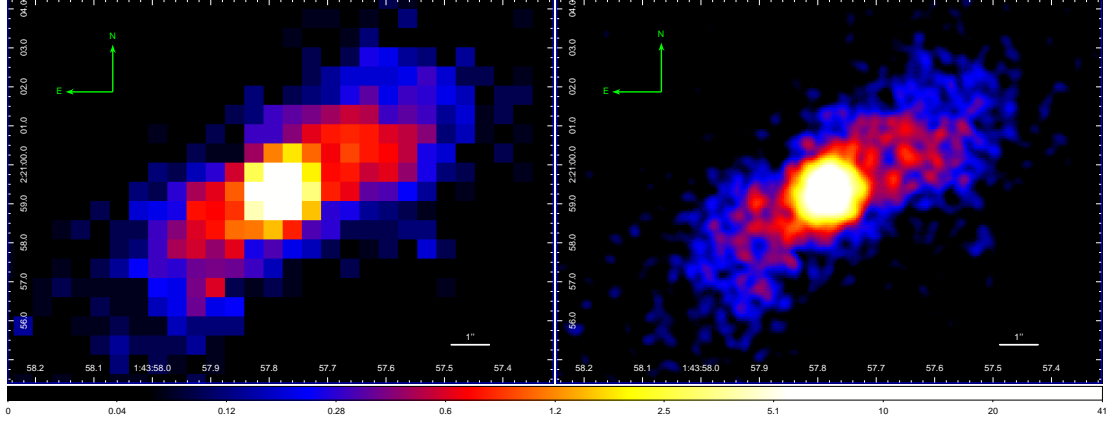


Fig. 1.— (left panel) Raw ACIS-S image of the soft X-ray emission (0.3 - 2 keV). (right panel) Same of left panel, but with subpixel binning (1/8 of the native pixel size) and a 2X2 FWHM gaussian filter smoothing.

line with an equivalent larger than 1 keV, yielding to the classification of Compton-thick object; high-resolution spectral analysis of RGS/*XMM-Newton* data by [Guainazzi & Bianchi \(2007\)](#) led to interpret the emission from this source in term of gas photoionized by the central AGN. Recently, two papers concerning the study of soft X-ray emission from Mrk 573 with ACIS/*Chandra* and RGS/*XMM-Newton* data have been published ([Bianchi et al. 2010](#); [Gonzalez-Martin et al. 2010](#)); they both agree in interpreting this emission as dominated by two photoionized phases, with the contribution of a collisional phase.

In this paper we present a detailed imaging and spectroscopic study of new Mrk 573 ACIS/*Chandra* data obtained as part of the CHandra survey of Extended Emission-line Regions in nearby Seyfert galaxies (CHEERS, [Wang 2010](#)). These new data, adding to the archival ones, reach an observation time of ~ 110 ks. With this deep observation the unmatched *Chandra* spatial resolution allows us to explore different region of Mrk 573 ENLR looking for a more comprehensive description of the underlying physical processes.

2. OBSERVATIONS AND DATA REDUCTION

2.1. ACIS/*Chandra* Data

Mrk 573 was observed by *Chandra* on 2006 November 18 for an exposure time of 40 ks (Obs. ID 07745, PI: Bianchi), and on 2010 September 16, 17 and 19, for an exposure time of 10, 53 and 17 ks respectively (Obs. IDs 12294, 13124, 13125); the last three observations were performed as

Table 1: Observations properties

Obs. ID	07745	12294	13124	13125	merged
Obs. Date	2006-11-18	2010-09-16	2010-09-17	2010-09-19	-
Exposure (ks)	35.07	9.92	52.37	16.76	114.12
Net Counts (0.3 - 2 keV) ^a	3173(57)	739(27)	3649(61)	1216(35)	8777(95)
Net Counts (2 - 10 keV) ^a	345(23)	79(12)	443(27)	160(15)	1027(41)

Notes:

^a Counts evaluated in a circular region of 15'' radius.

part of the CHEERS survey. Level 2 event data were retrieved from *Chandra* Data Archive² and reduced with the Chandra Interactive Analysis of Observations (CIAO; [Fruscione et al. 2006](#)) 4.3 software and the *Chandra* Calibration Data Base (CALDB) 4.4.3, adopting standard procedures.

Time intervals of background flares exceeding 3σ of the quiet level were excluded using the LC_SIGMA_CLIP task in source free regions of each observation; net exposure times are reported in Table 1. The nucleus has no significant pile up as suggested by the CIAO PILEUP_MAP tool.

We produced a merged image of the four observations, to take advantage of the longer exposure time and identify fainter signatures; we used the WAVDETECT task to identify point sources in each observation, then we used REPROJECT_ASPECT task to modify the aspect solution minimizing position differences between the sources found, and finally merged the images with the MERGE_ALL script.

2.2. Optical and Radio Data

To compare the soft X-ray emission with optical and radio structures, we retrieved *HST* and *VLA* images of Mrk 573. In particular, we retrieved from the Hubble Legacy Archive³ the *HST*/WFPC2 narrow band image with the FR533N filter, obtained as part of the GO program 6332 (PI: Wilson) on 1995 November 12, with the source located in the camera to track the [O III] λ 5007 emission line ([Falcke et al. 1998](#); [Schmitt et al. 2003](#)); this image was aligned to the X-ray images by matching the brightest pixel of the nuclear source in both images. The [O III] image shows the bright nucleus with two bright spots at $\sim 1''$ and $\sim 0.7''$ in the NW and SE directions, respectively; we also see two jet arcs in the two cones, the brighter inner arcs at $\sim 2''$ and $\sim 1.5''$ and the fainter

²<http://cda.harvard.edu/chaser>

³<http://hla.stsci.edu/hlaview.html>

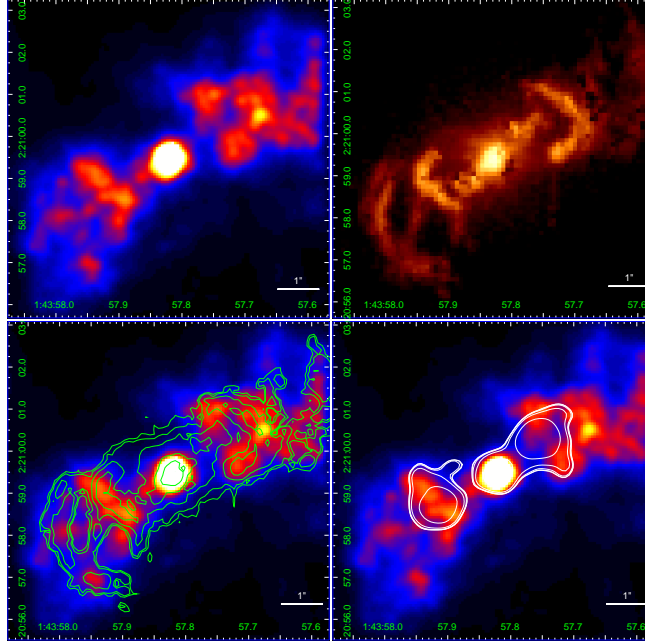


Fig. 2.— (Upper-left panel) PSF-deconvolved ACIS image (0.3 – 2 keV) using the EMC2 method, with subpixel binning (1/8 of the native pixel size) and a 2X2 FWHM gaussian filter smoothing. The same image is presented in the lower-left and lower-right panels with overlaid the *HST* [O III] and radio *VLA* 6 cm contours, respectively. (Upper-right panel) *HST* [O III] image.

outer arcs at $\sim 4''$ and $\sim 3''$ from the nucleus in the NW and SE directions, respectively (see Figure 2, see also Ferruit et al. 1999; Quillen et al. 1999).

We retrieved from the NASA/IPAC Extragalactic Database (NED⁴) the image of the 6 cm (5 GHz) observation performed in 1985 March 3 in A array configuration; this image clearly shows a central nucleus with a size $\sim 1''$ and two side lobes of similar size aligned with the NLR (Ulvestad & Wilson 1984; Falcke et al. 1998).

3. IMAGE ANALYSIS

Imaging analysis was performed with the subpixel event repositioning (SER) procedure (Li et al. 2003) and without pixel randomization, to take advantage of the telescope dithering and allow subpixel binning of the images, using pixel scale smaller than the native one $0.492''$ of the *Chandra*/ACIS detector (see, e.g., Harris et al. 2004; Siemiginowska et al. 2007; Perlman et al.

⁴<http://ned.ipac.caltech.edu/>

2010; Wang et al. 2011a); Figure 1 shows the merged images, with a comparison between the native ACIS pixel and the subpixel binning with 1/8 of the native pixel size. As shown in Figure 2, while the radio emission appears more compact than the soft X-ray emission, the latter shows a remarkable coincidence with the ENLR as mapped by [O III] emission, suggesting a common physical origin.

3.1. Comparison with *Chandra* PSF

We performed Point Spread Function (PSF) simulations with Chandra Ray Tracer (ChaRT⁵, Carter et al. 2003) taking into account the source spectrum, exposure time and off-axis angle; while the hard band images (2 – 10 keV) show a point-like structure consistent with the simulated PSF, the soft band images (0.3 – 2 keV) show extended morphology that closely resembles that of the NLR, as mapped by the [O III] emission (see Figure 2).

In Figure 3 we show radial profiles of the soft X-ray emission for the NW and SE direction in comparison with the simulated PSF in the same band; while the nuclear emission in the inner $\sim 1''$ is comparable with the PSF, the diffuse emission extends in both directions up to $\sim 10''$.

3.2. Image Deconvolution

We applied to the merged images of the soft emission two different PSF-deconvolution algorithms, namely the Richardson-Lucy (R-L) (Richardson 1972; Lucy 1974) and the Expectation through Markov Chain Monte Carlo (EMC2) (Esch et al. 2004; Karovska et al. 2005, 2007); while both methods show a similar extended morphology in the deconvolved images, the R-L algorithm yields a more grainy image reconstruction with respect to EMC2; the latter results are presented in Figure 2. In particular, in the upper panels we show a comparison between the reconstructed ACIS image with the subpixel binning (1/8 of the native pixel size) and the [O III] image: the soft X-ray extended emission clearly shows structures in correspondence with the optical optical arcs (Hollis et al. 1997); this correspondence is more clearly shown in the lower panels of the same figure, where [O III] and radio contours are overlaid to the soft X-ray emission. The X-ray structures show a striking coincidence with the optical features, indicating an interesting interplay between radio ejecta, optical and X-ray emissions; in particular we see soft X-ray structures lying in coincidence or just in front of the inner [O III] arcs, the latter wrapping around the outer radio lobes.

⁵<http://cxc.harvard.edu/chart/>

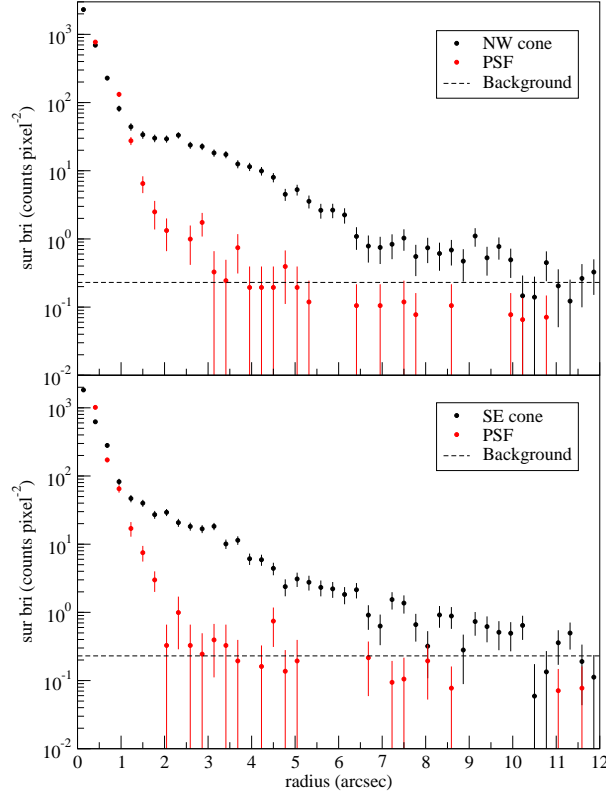


Fig. 3.— Radial profiles of the ionizing cones (black dots) in comparison with the simulated PSF (red dots) in the 0.3 – 2 keV range.

3.3. Diffuse emission

The deep exposure reached with CHEERS observations (~ 110 ks) allows us to explore fainter features of the diffuse emission; to enhance these, we applied the adaptive smoothing procedure on the merged image of the soft X-ray emission with the `csmooth` tool (Ebeling et al. 2006), using a minimum and maximum significance S/N level of 2.5 and 3.5, respectively; this smoothing procedure allow us to enhance fainter, extended features of the diffuse emission. The smoothed image is presented in Figure 4; the bicone emission appears to extend to ~ 6 kpc in the NW direction and ~ 7 kpc in the SE direction, as also confirmed by the extended radial profiles presented in Figure 5.

We then focused on the region that is supposed to be obscured by the dusty torus in the AGN unified model; the region we studied is defined by a bicone with P.A. = 34° , a half opening angle of 55° , and inner and outer radii of $1.5''$ and $12''$, as shown in Figure 7. We found in this region a

significant emission ($SNR \approx 22$) in the soft X-ray emission of all observations, extending to $\sim 8''$ as shown in Figure 6; we will discuss the emission from this region in detail in Sect. 7.

4. SPECTRAL ANALYSIS

In order to study the X-ray properties of the diffuse emission we extracted spectra with the CIAO `SPEXTRACT` task from three different regions centered at RA 01:43:57.78, DEC +02:20:59.32: the nuclear region, defined as a circular region with a $1''$ radius; the NW and SE cones region, both defined as cones with an inner radius of $1.5''$ and a half opening angle of 30° , centered at P.A. $= -56^\circ$ and 124° respectively. Based on the radial profiles shown in Figure 3 we decided to extract cones spectra out to $12''$, where the emission of the cones reaches the background level. For spectra extracted from the nuclear region we applied the point-source aperture correction to `SPEXTRACT` task. The extraction regions are shown in Figure 7.

To make use of the χ^2 fit statistic we binned the spectra to obtain a minimum of 20 counts per bin using the `SPEXTRACT` task; in the following, errors correspond to the $1-\sigma$ confidence level for one interesting parameter ($\Delta\chi^2 = 1$). In all the spectral fits we included photo-electric absorption by the Galactic column density along the line of sight $N_H = 2.52 \times 10^{20} \text{ cm}^{-2}$ (Kalberla et al. 2005); we also tried to evaluate intrinsic absorption but without significant results.

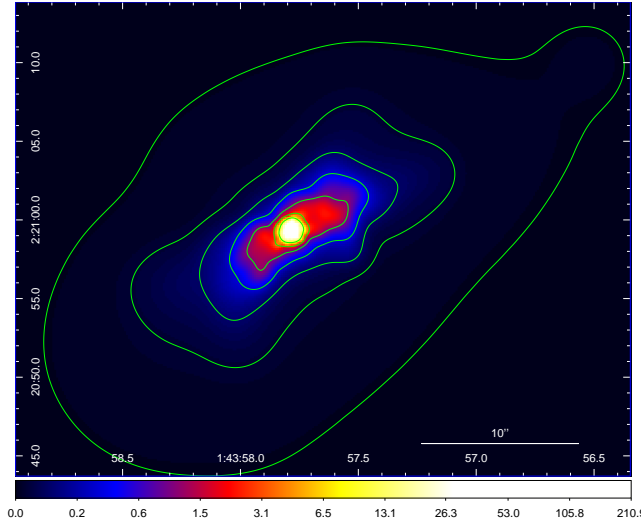


Fig. 4.— Adaptive smoothing applied to subpixel binned ACIS-S image of the soft X-ray emission (0.3 - 2 keV); showing extended emission up to ~ 6 kpc. Contours correspond to seven logarithmic intervals in the range of 0.003 – 5% with respect to the brightest pixel.

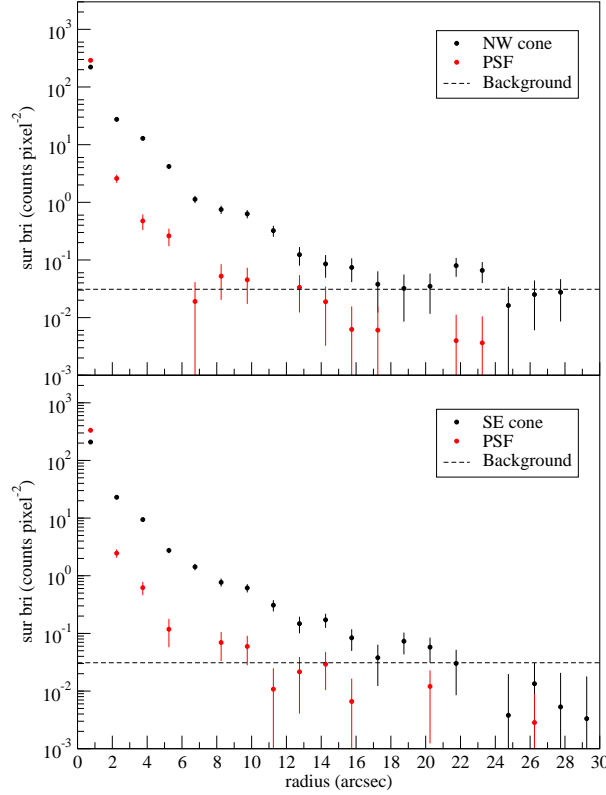


Fig. 5.— Extended radial profiles of the NW (top panel) and SE (bottom panel) cones (black dots) in comparison with the simulated PSF (red dots) in the 0.3 – 2 keV range.

4.1. Nuclear spectra

The soft X-ray emission from Seyfert galaxies can be effectively described in terms of several emission lines with a small power-law continuum contribution. We therefore performed the spectral analysis of emission of Mrk 573 with the XSPEC software (ver. 12.7.0⁶, [Arnaud 1996](#)) fitting the soft (0.3 – 2 keV) spectra of different observations in the nuclear region using a phenomenological model constituted by a power-law photon index fixed to $\Gamma = 1.8$ (a typical value for Seyfert galaxies, see [Bianchi et al. 2009](#)), plus several red-shifted emission lines adopting as a reference the lines measured on the 2006 November 18 observation (Obs. ID 07745) by [Gonzalez-Martin et al. \(2010\)](#) in RGS/*XMM-Newton* high resolution spectra; due to high counts in this region we were able to obtain acceptable fits for all observations. To obtain better statistics, we also performed simultaneous fits on data from observations from CHEERS (Obs. IDs 12294, 13124 and 13125) as

⁶<http://heasarc.nasa.gov/xanadu/xspec/>

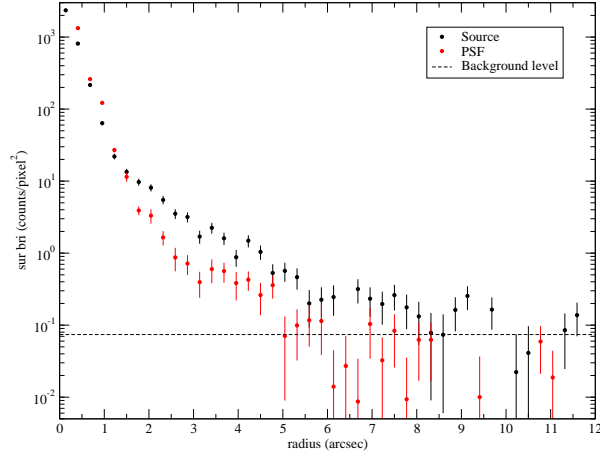


Fig. 6.— Radial profiles of the cross cone region (black dots) in comparison with the simulated PSF (red dots) in the 0.3 – 2 keV range.

well as for all observations (CHEERS obs. + Obs. ID 07745). Fit results are in general agreement with previous results by [Bianchi et al. \(2010\)](#) and [Gonzalez-Martin et al. \(2010\)](#), and are presented in the Appendix.

Nuclear spectra are dominated by C v He γ , C vi Ly β , N vii Ly α , O vii triplet, O viii Ly α , O vii RRC, Fe xvii and Ne ix triplet, although significant variations are observed between observations. In particular, flux in 0.3 – 2 keV band is higher in obs. 07745, with a value of 5.3×10^{-13} erg cm $^{-2}$ s $^{-1}$, than in CHEERS observations, where it reaches a value of 4.05×10^{-13} erg cm $^{-2}$ s $^{-1}$; these variations reflects in the poor fit obtained with merged observation ($\chi^2 = 1.63$).

High resolution spectroscopic analyses performed by [Bianchi et al. \(2010\)](#) and [Gonzalez-Martin et al. \(2010\)](#) on RGS/*XMM-Newton* data suggest that the soft X-ray spectrum originate from photoionized and photoexcited plasma with the contribution of collisionally excited plasma. In order to evaluate the contribution of different plasma phases to the total emission we performed spectral fitting of the nuclear spectra making use of self-consistent photoionization models. For this purpose we produced xSPEC grid models with the CLOUDY⁷ c08.01 package, last described by [Ferland et al. \(1998\)](#). We assumed the ionization source to be an AGN continuum (with a big bump temperature $T = 10^6$ K, a X-ray to UV ratio $\alpha_{ox} = -1.30$ and a X-ray component spectral index $\alpha = -0.8$) illuminating a cloud with plane-parallel geometry with constant electron density $n_e = 10^5$ cm $^{-3}$; note that the fits are expected to be quite insensitive to n_e ([Porquet & Dubau 2000](#)). The grid of models so obtained are parametrized in terms of the ionization parameter U (varying in

⁷<http://www.nublado.org/>

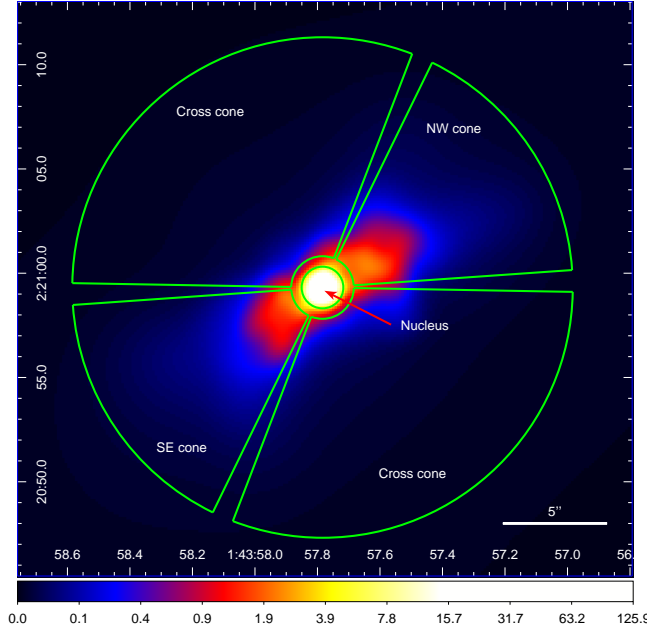


Fig. 7.— Adaptive smoothing applied to subpixel binned ACIS-S image of the soft X-ray emission (0.3 - 2 keV) with overlaid the extraction regions considered in the text.

the range $\log U = [-3.00 : 2.00]$ in steps of 0.25) and the hydrogen column density N_H (expressed in cm^{-2} varying in the range $\log N_H = [19.0 : 23.5]$ in steps of 0.1), taking into account only the reflected spectrum from the illuminated face of the cloud (Bianchi et al. 2010; Marinucci et al. 2011).

Since the nuclear emission significantly extends beyond the soft band, we performed nuclear spectral fits in the 0.3 – 10 keV energy range, adopting, in addition to the photoionization model, a pure neutral reflection component with the `PEXRAV` `XSPEC` model with the photon index fixed to 1.8 and the cosine of inclination angle fixed to 0.45; we also added to our model the Si $K\alpha$, S $K\alpha$ and Fe $K\alpha$ lines (see Bianchi et al. 2010). The results of the fitting procedures are presented in the Appendix.

Poor fits are obtained with a single phase ionized plasma; the best fit models actually require two photoionized phases, respectively with a higher and lower values of the ionization parameter. The higher ionization phase features values of $\log U_1 \approx 1$ and $\log N_{H1} \approx 21$ for the ionizing parameter and the hydrogen column density, both in obs. 07745 and in CHEERS observations; the best fit values for the less ionized phase are $\log U_1 \approx -0.7$ in all observations, and $\log N_{H1} \approx 20$ and $\log N_{H1} \approx 21$ in obs. 07745 and in CHEERS observations, respectively. We also added to our fitting model a thermal component, included with the `APEC` `XSPEC` model, looking for the thermally

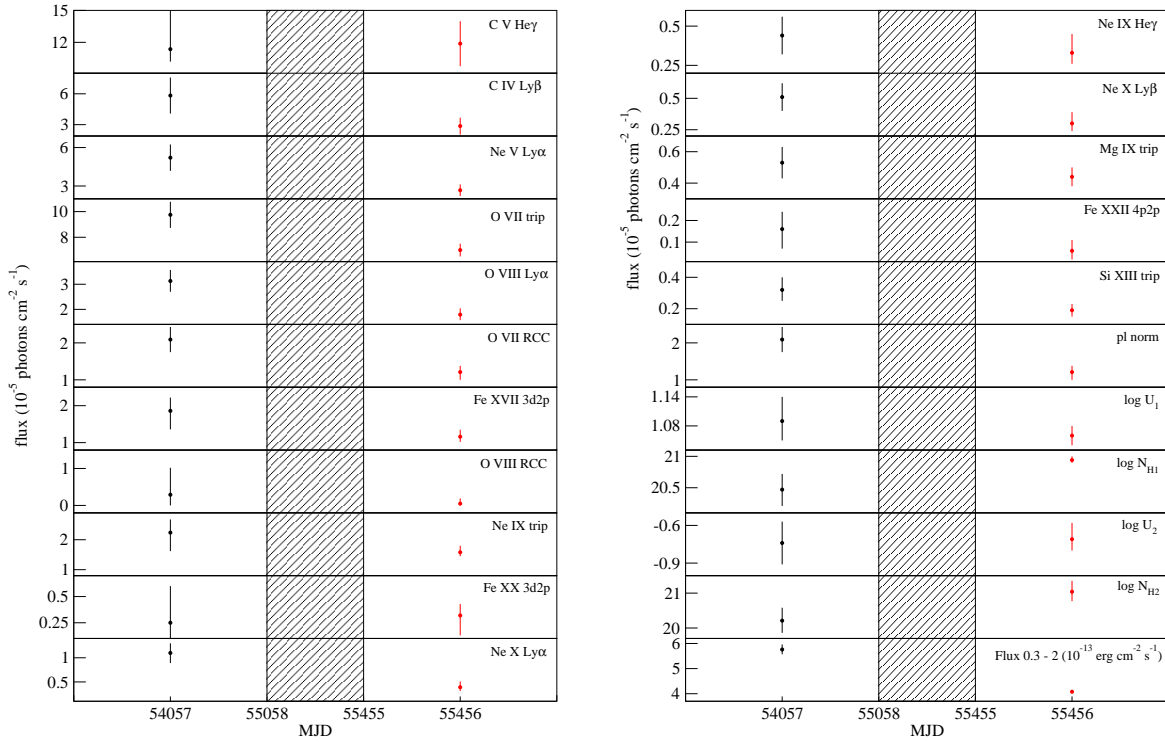


Fig. 8.— Variation of nuclear spectral components between obs. 07745 (black point) and CHEERS obs. (red point). The decrease in the soft X-ray flux appears to be related with the decrease of some emission lines and the increase of the hydrogen column density of the photoionized phases.

ionized plasma found by [Gonzalez-Martin et al. 2010](#) and [Bianchi et al. 2010](#), but the best fit models do not require this component. In fact, a model that includes a thermal component in the nuclear region does not provide better χ^2 values, and is not able to constrain neither the plasma temperature nor the APEC component normalization, yielding only upper limits for the thermal component flux F_C : in particular, we find for CHEERS obs. $F_{C(0.3-10)} < 0.06 \times 10^{-13} \text{ erg cm}^{-2} \text{ s}^{-1}$, while for all merged obs. we find $F_{C(0.3-10)} < 0.08 \times 10^{-13} \text{ erg cm}^{-2} \text{ s}^{-1}$. In sum, we have no significant indications that the collisionally ionized plasma is located in the nuclear region; we cannot exclude that this component may be located outside the nucleus, inside the ionization cones (see Sects. 4.2 and 5).

The decrease in nuclear flux across the observations is observed also with the photoionization model. In fact, while in obs. 07745 we have for the 0.3 - 2 keV flux a value of $5.8 \times 10^{-13} \text{ erg cm}^{-2} \text{ s}^{-1}$, for the CHEERS obs we have $4.1 \times 10^{-13} \text{ erg cm}^{-2} \text{ s}^{-1}$. A slight decrease in flux is also observed in the 2 -10 keV band (where we have a flux value of $3.7 \times 10^{-13} \text{ erg cm}^{-2} \text{ s}^{-1}$ for obs. 07745 and $3.4 \times 10^{-13} \text{ erg cm}^{-2} \text{ s}^{-1}$ for CHEERS obs.) added to a decrease in the reflection

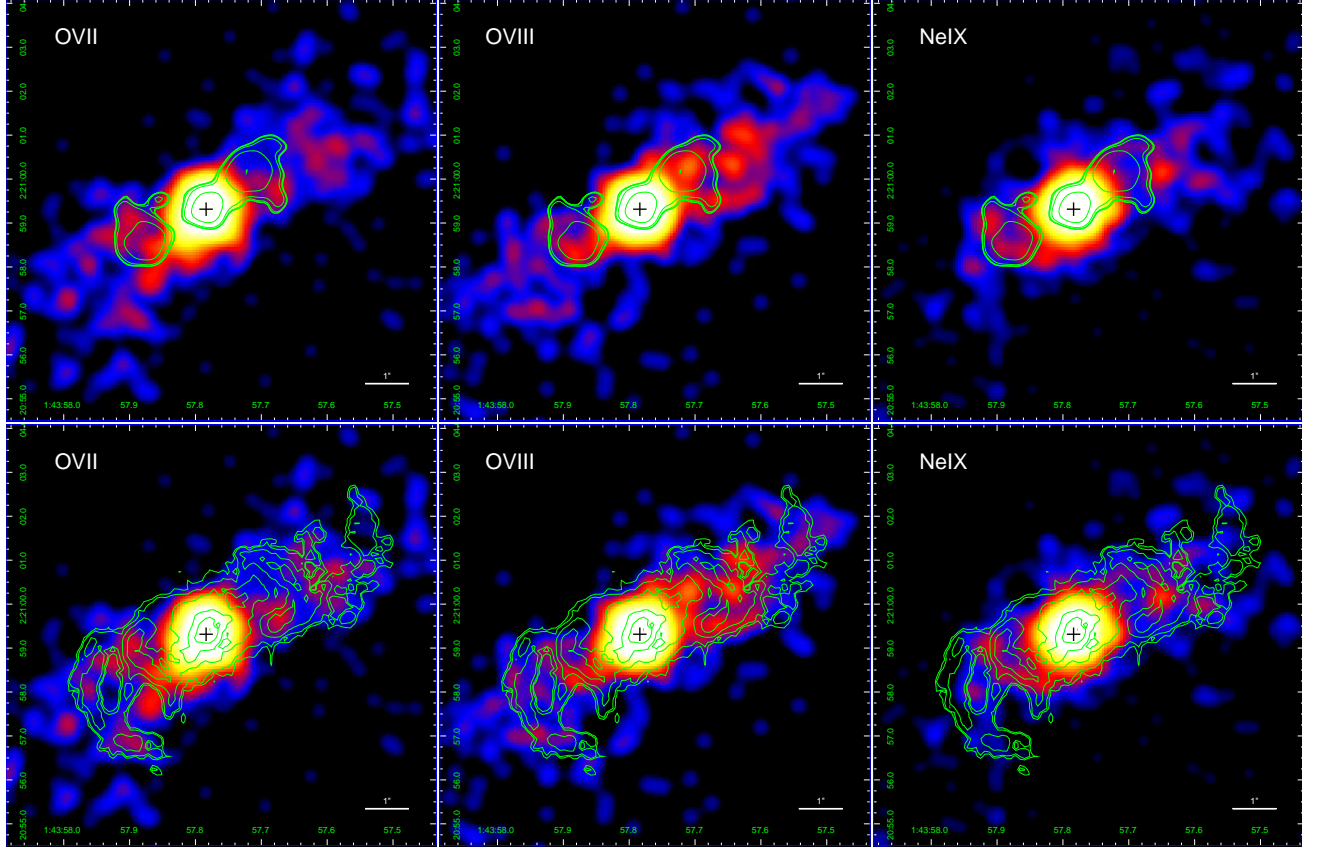


Fig. 9.— Emission-line maps of the central 3.5 kpc of Mrk 573: from left to right are shown the O VII triplet (0.53 - 0.63 keV), O VIII Ly α (0.63 - 0.68 keV) and Ne IX triplet (0.90 - 0.95 keV) maps, with overlaid the 6 cm radio contours (upper panel) and [O III] contours (lower panel). The images are rebinned to 1/8 of the native pixel size and smoothed with a 3X3 FWHM gaussian filter. The nucleus position is marked with the black cross.

component normalization; anyway, the fluxes are compatible within uncertainties.

To study nuclear flux variations we plot in Fig. 8 fluxes of the different spectral components used in our phenomenological model, as well as ionization parameters and hydrogen column densities obtained with the photoionization model for different observations. We clearly see that the nuclear flux decrease is marked by a significant decrease in several emission lines (such as Ne v Ly α , O VII triplet, O VIII Ly α , O VII RCC and Ne x Ly α ,) as well as in the power-law normalization; on the other hand, while ionization parameters are approximatively the same, there is a significant increase in the hydrogen column density in both photoionized phases.

The decrease in soft X-ray nuclear flux seems so to be related to an increased hydrogen column density of the two photoionized phases, while the hard X-ray flux does not seem to respond

to these variations, indicating that N_H variations are not due to changes in plasma ionization state (see [Risaliti et al. 2002](#)).

4.2. Cone spectra

We performed spectral fitting of the soft X-ray emission in each cone for different observations, adopting the same models described in Sect. 4.1; to avoid contaminations from the nuclear continuum we evaluated the contribution from the PSF wings in the cone regions and subtracted it from the cones spectra. This nuclear contribution is $\sim 0.8\%$.

To evaluate the emission lines fluxes we adopted the same phenomenological model used above. These results also confirm results by [Bianchi et al. \(2010\)](#) and [Gonzalez-Martin et al. \(2010\)](#), and are presented in the Appendix.

The spectra appear to be dominated by C vi, O vii triplet, O viii, O vii RRC and Ne ix triplet; while most lines show almost the same flux on both cones, there is some evidence of stronger a O viii RRC in the NW cone with respect to the SE one, as already reported by [Gonzalez-Martin et al. \(2010\)](#), while and opposite behavior is observed for Ne ix triplet. Bolometric flux and line fluxes in both cones do not show strong variations between different observations, as expected given the size of the emitting regions.

We then proceeded to fit the cone spectra with the photoionization model described in Sect. 4.1; the results of the fitting procedure are shown in Table 6 and Figure 16. Again, poor fits are obtained with a single phase ionized plasma; the best fit models actually require two photoionized phases, respectively with a higher and lower values of the ionization parameter. Due to low counts, the latter phase results essentially unconstrained, so we fixed its parameters to their best fit values of $\log(N_{H1}) = 20$, and $\log(U_2) = -2$ and in the NW cone and $\log(U_2) = -1$ in the SE cone. In particular, for Obs. ID 07745 we find values of $\log U_1 \approx 0.3$ for both cones, and $\log(N_{H1}) = 20.6$ and $\log(N_{H1}) = 20.1$ for NW and SE cone, respectively; Obs. ID 13124 shows parameter values similar to 07745 in the NW cone, while in the SE cone we find a slightly higher ionization parameter, but still compatible within $1-\sigma$ error. The simultaneous fit of CHEERS observation yields $\log U_1 = 0.3$ and $\log(N_{H1}) = 20.2$ for the NW cone, and $\log U_1 = 0.5$ and $\log(N_{H1}) = 20.5$ for the SE cone. For these observations the more ionized phase appear to be brighter than the less ionized one in the NW cone, while in the SE cone the two phases show similar fluxes.

In almost all observations, the best fit models require a thermal component (included with an `APEC XSPEC` model); the exception is constituted by observation 07745 on the SE cone, but this is probably due to the low statistic being this the region with the lowest counts. All other fits require this thermal component with temperature $kT \approx 0.8$ keV and $kT = 1.0$ keV in the NW and SE

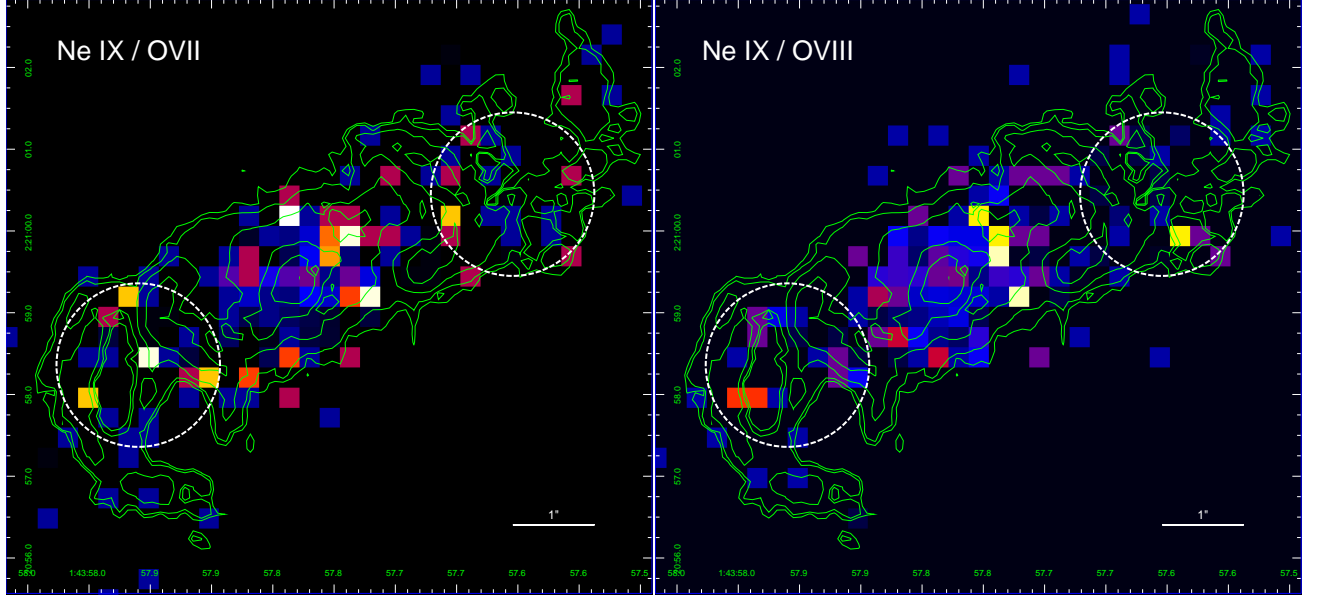


Fig. 10.— Ratio Ne ix / O vii maps (left panel) and Ne ix / O viii (right panel) with overlaid [O iii] (subpixel binning 1/2 of the native pixel). The high ionization regions used for spectral extraction are shown in white.

cone, respectively. With the exception of SE cone in observation 07745, the various phases do not show significant flux variations between different observations, and the total flux for the two cones appear to be unchanged between various observations within $1\text{-}\sigma$ error.

We can therefore conclude that a two-phases photoionized plasma is diffused over the two cones, with the presence of a thermal component.

5. SPATIAL DISTRIBUTION OF SPECTRAL FEATURES

Summarizing the results obtained in the spectral fits presented in Sects. 4.1 and 4.2, the nuclear region is characterized by highly photoionized plasma ($\log U \approx 1$), while the two cones are characterized by mildly photoionized plasma ($\log U \approx 0.3$ in the NW cone and $\log U \approx 0.5$ in the SE cone) and the presence of collisionally ionized plasma at a temperature ≈ 1 keV.

CHEERS observations of Mrk 573 reveal a detailed structure of the diffuse emission that is morphologically coincident with the ENLR as mapped by [O iii] and suggest an interplay between radio ejecta, the optical and the soft X-ray emissions (see Figure 2); the inner optical arcs appear wrapped around the radio knots, as resulting from shock interactions between the radio jets and the galactic plane, and the X-ray emission is enhanced in front of these knots, suggesting the presence

of collisionally ionized gas, a picture analogous to what is observed in NGC 4151 (Wang et al. 2011b).

To further investigate these features, we produced maps of the X-ray emission in three energy bands corresponding to some of strongest emission lines, namely the blended O VII triplet (0.53 - 0.63 keV), O VIII Ly α (0.63-0.68 keV) and Ne IX triplet (0.90 - 0.95 keV), and present them in Figure 9. As already observed by Bianchi et al. (2010) the O VII emission appears to be slightly more extended in the SE cone with respect to the O VIII Ly α , while in the NW cone we observe an opposite behavior. The Ne IX maps shows spots of enhanced emission in front of the radio lobes; these spots are also present in the ratio map of lines emission shown in Figure 10, where we present ratios of Ne IX to O VII and O VIII emissions, tracing the higher ionization gas; these maps shows the central highly ionized region correspondent with the nuclear region, and two nearly symmetrical regions with $\sim 1''$ radius of increased ionization, lying in front of the radio knots at the interface between the optical arcs.

These region of increased ionization are also clearly shown in Figure 11, where we plot variations of the ratio of [O III] to 0.5 - 2 keV flux along with the distance from the nucleus, where an average conversion factor of 8.7×10^{-12} erg cm $^{-2}$ s $^{-1}$ counts $^{-1}$ s, obtained by the various spectral fits we performed, is used to convert net counts in the 0.5 - 2 keV band into flux. At radii greater than 1 pc, the ratio of [O III] to soft X-ray flux for a single photoionized medium is expected to approximatively have a power law dependence on the radius, depending on the radial density pro-

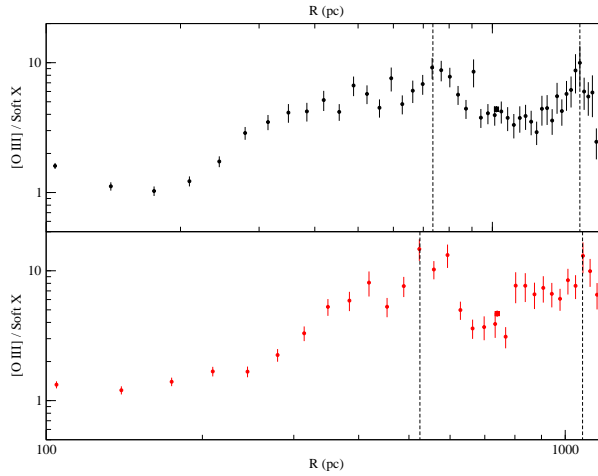


Fig. 11.— Variation of the [O III] to soft X-ray flux ratio, in the NW (upper panel) and SE (lower panel) cone as a function of the distance from the nucleus. The vertical dashed lines represent the location of the inner and outer optical arcs, and the squares represent the regions of increased ionization shown in Figure 10.

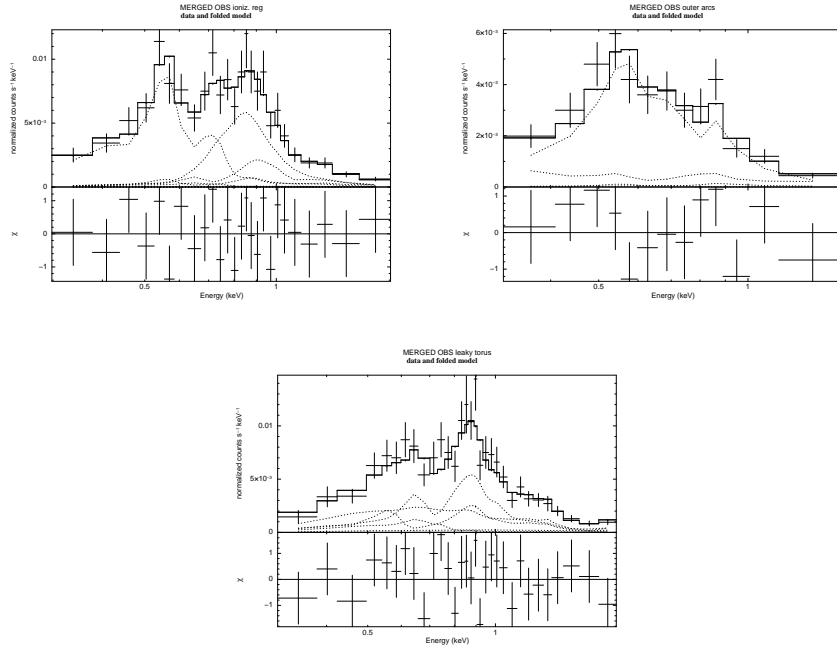


Fig. 12.— Merged *Chandra* ACIS-S 0.3 – 2 keV spectra of the regions discussed in Sect. 5 and 6, with best fit photoionization models.

file (Bianchi et al. 2006). The trends shown in Figure 11 can be roughly sketched with the inner $\sim 1''$ region corresponding to the nuclear highly photoionized phase with $\log U = 1$, and two outer regions corresponding to the mildly photoionized cones with $\log U = 0.3$ in the NW direction and $\log U = 0.5$ in the SE direction, respectively; in more detail we can see that the roughly constant ratio in the cones features significant dips at the interface between the optical arcs (see also Gonzalez-Martin et al. 2010). These dips, correspondent to regions of enhanced ionization seen in the ratio maps (see Figure 10), may be due to enhanced X-ray emission due to shock heating adding to photoionization, as already observed in NGC 4151 (Wang et al. 2011b).

In order to investigate the nature of the various plasma phases in these regions of enhanced ionization (shown in Figure 10) we extracted here soft X-ray spectra and fitted them adopting the photionization model described above, taking into account the nuclear contribution to these regions; in order to have enough counts and allow acceptable fits we extracted spectra from all observations and combined them with the *SPEXTRACT* tool. Fits results are presented in Table 2 and Figure 12.

The best fit model requires a highly ionized phase with $\log U_1 \sim 1.3$ and a low ionized phase with $\log U_2 \sim -0.9$; due to the low counts the hydrogen column densities were fixed to their best fit values of 20. The model also requires a thermal component with $kT \approx 0.8$ keV, which

we interpret as the origin of the enhanced X-ray emission. To further check the location of the collisionally ionized phase found in the cones we performed an analogous analysis on the [O III] outer arcs; a good fit is obtained with two photoionized phases, while the inclusion of a thermal component is not statistically required, as the fitting procedure is not able to constrain neither the temperature nor the normalization of the APEC component, and only yields an upper limit on its flux $< 0.02 \times 10^{-13} \text{ erg cm}^{-2} \text{ s}^{-1}$ (see Table 2 and Figure 12). We can therefore conclude that the thermal component is not diffused over the cones, but is found in front of the radio knots, at the interface between the optical arcs.

6. DISCUSSION

CHEERS observations of Mrk 573 show soft X-ray emission characterized by a bright nucleus and a diffuse component extending along the ionizing bicone up to ~ 7 kpc, doubling the size reported in previous works (Gonzalez-Martin et al. 2010). The spectral analysis of the diffused emission points to the presence of a thermal component that can be interpreted as collisionally ionized gas related to radio ejecta; moreover, significant extended emission up to ~ 3 kpc is

Table 2: Best fit photoionization models for other regions (merged observations).

Region	Ionization Regions	[O III] outer arcs	torus region
Net Counts (0.3 - 2 keV)	691(26)	308(18)	733(28)
Model Parameter			
$\log(U_1)$	$1.33^{1.64}_{1.02}$	$0.18^{0.27}_{0.06}$	$1.08^{1.13}_{0.86}$
$\log(N_{H1})$	20^*	$20.07^{20.45}_{19.70}$	19^*
$F_{1(0.3-2)}^a$	$0.04^{0.07}_{0.01}$	$0.17^{0.19}_{0.15}$	$0.12^{0.15}_{0.10}$
$\log(U_2)$	$-0.85^{-0.60}_{-0.99}$	-2^*	$1.29^{1.36}_{1.09}$
$\log(N_{H2})$	20^*	20^*	$23.32^{23.47}_{23.10}$
$F_{2(0.3-2)}^a$	$0.26^{0.29}_{0.20}$	$0.06^{0.09}_{0.03}$	$0.13^{0.16}_{0.09}$
kT^b	$0.76^{0.87}_{0.65}$	-	-
$F_{C(0.3-2)}^a$	$0.08^{0.11}_{0.06}$	-	-
$\chi^2(\text{dof})$	$0.72(20)$	$0.98(9)$	$0.91(26)$
$F_{0.3-2}^a$	$0.42^{0.45}_{0.39}$	$0.23^{0.25}_{0.21}$	$0.25^{0.00}_{0.00}$

Notes:

^a Unabsorbed flux in units of $10^{-13} \text{ erg cm}^{-2} \text{ s}^{-1}$.

^b Plasma temperature in keV.

observed in the cross-cone direction where the obscuring torus is expected to be according to the AGN unified model. In this section we will discuss these two aspects of the diffuse emission.

6.1. Energetic content of the collisionally ionized gas

Previous work on Mrk 573 (Gonzalez-Martin et al. 2010; Bianchi et al. 2010) agree that soft X-ray diffuse emission from this source can be interpreted as originating from mildly photoionized plasma with the presence of a collisionally ionized phase; with new, deep CHEERS observations we are able to conclude that the collisionally ionized phase found in Section 4.2 is not diffused over the cones, but is actually located in front of the radio knots, at the interface between the optical arcs.

The collisionally ionized phase can be interpreted as the result of a shock interaction between radio ejecta and the galactic plane, because this is the expected location of the interaction between the ionizing cones and the galactic plane (see Figure 2).

The electron density and thermal pressure of the collisionally ionized gas can be estimated through the normalization of the APEC component, that is, its emission measure

$$EM = 10^{-14} \frac{n_e n_H V \eta}{4\pi [D_A (1+z)]^2},$$

where n_e and n_H are the average electron and hydrogen density, V is the emitting region volume, η is the filling factor and D_A is the angular diameter distance to the source. On assuming $n_e = 1.2 n_H$, a filling factor $\eta \approx 1$ and a spherical shape for the emitting regions, one obtains $n_e = 0.14 \text{ cm}^{-3}$ and a thermal pressure $p_{th} = 3.8 \times 10^{-10} \text{ dyne cm}^{-2}$; if the collisionally ionized gas is assumed to be diffused over the whole cones one obtains a thermal pressure $1.3 \times 10^{-9} \text{ dyne cm}^{-2}$ in agreement with the result found by Bianchi et al. (2010). It is interesting to compare the thermal pressure with the pressure of radio jets; a lower limit to it can be estimated on assuming energy equipartition between particles and magnetic field (see, e. g., Hardcastle et al. 2004). We model the two radio knots as spheres with a radius $\sim 200 \text{ pc}$ filled with electrons featuring a power law energy distribution with an index $r = 2.4$ (an average between the indexes measured by Falcke et al. 1998) and Lorentz factors $2 < \gamma < 10^5$; assuming that the 6 cm luminosities reported by Bianchi et al. (2010) are due to synchrotron emission from this electron population we obtain jet pressures due to electrons energy density of $3 \times 10^{-11} \text{ dyne cm}^{-2}$ and $4 \times 10^{-11} \text{ dyne cm}^{-2}$ for the NW and SE lobe, respectively, about 10 times smaller than the evaluated thermal pressure in the regions of enhanced ionization. Instead, the thermal pressures are comparable with the pressures due to the total energy density $7/3 U_B$ (where U_B is the magnetic field energy density), which are $1.5 \times 10^{-10} \text{ dyne cm}^{-2}$ and $2.2 \times 10^{-10} \text{ dyne cm}^{-2}$ for the NW and SE lobe, respectively. These

pressures are comparable with p_{th} , suggesting that shocks of radio ejecta with ISM are likely to be responsible of gas heating we locate in front of the radio lobes. Nevertheless, due to large uncertainties in these estimates, a sharp conclusion cannot be drawn.

The thermal energy associated to the collisionally ionized gas is evaluated as $E_{th} = 2.7 \times 10^{54} \text{ erg s}^{-1}$, corresponding to a cooling time $t_{cool} = E_{th}/L_C \approx 1.6 \times 10^7 \text{ yr}$ (where L_C is the luminosity of the thermal component); on the other hand, the local sound speed is $c_s \sim 600 \text{ km s}^{-1}$, comparable with the shock velocity estimated assuming strong shock conditions with $v_{sh} \approx 100 (kT/0.013 \text{ keV})^{1/2} \text{ km s}^{-1}$ (Raga et al. 2002) as 800 km s^{-1} , and yields a crossing time of the radio knots $t_{cross} = 8.6 \times 10^5 \text{ yr}$, about 40 times shorter than the cooling time, thus not requiring extra heating sources. The jet luminosity can be evaluated using the $P_{jet} - P_{radio}$ relation in Cavagnolo et al. (2010) and the 1.4GHz radio luminosity $\nu L_\nu = 4.1 \times 10^{37} \text{ erg s}^{-1}$ (Condon et al. 1998), to obtain $P_{jet} \approx 1.3 \times 10^{42} \text{ erg s}^{-1}$. The jet luminosity can be compared with the jet kinematic power, whose lower limit can be evaluated as $L_K \gtrsim E_{th}/t_{cross} \approx 2 \times 10^{41} \text{ erg s}^{-1}$, indicating that $\gtrsim 15\%$ of the jet power is deposited in the ISM.

6.2. Emission from the cross cone region

Another interesting feature of the diffused emission is the significant emission in the cross cone direction. As recalled before, such an emission is not expected in the presence of a dusty torus, and may therefore be due to nuclear radiation leaking through a clumpy structure, like a warm highly ionized medium (WHIM, Elvis 2000). Cross-cone emission was also found in NGC 4151 by Wang et al. (2011c), where the authors interpreted it as the result of leaking nuclear continuum through a filtering structure with a covering factor $\sim 10\%$.

As recalled in Sect. 1, Fischer et al. (2010) developed a kinematic model of Mrk 573 NLR, and concluded that the apparent bicone half opening angle of $\sim 30^\circ$ is likely due to the intersection with the galactic plane of a much wider ionizing bicone, with an intrinsic half opening angle $\sim 53^\circ$, which is close to the 60° expected in the unifying structure for the inner quasar regions presented by Elvis (2000). In order to test such a model we extracted the spectrum of the soft emission in the region shown in Figure 7, and fitted with a photoionization model; due to faintness of the diffuse emission in this region, contamination from nuclear emission has been taken into account and evaluated to $\sim 3\%$. In order to represent the WHIM structure we included in the model a transmitted component to mimic radiation arising from the WHIM itself and a reflected component that takes into account the leaking radiation illuminating the ISM; the result of this fit is presented in Table 2 and Figure 12.

The best fit model requires for the WHIM component a ionization factor of about 1.3 (to be compared with the value of 2 found for NGC 5548 by Mathur et al. 1995) and a hydrogen column density of 23.3, somewhat higher than the 22.5 value expected for the WHIM model. For the filtered component the hydrogen column density has been fixed to its best fit value of 19, while the ionization parameter is found to be ~ 1.1 ; such a high value may be due to lower density of the illuminated medium. However the low counts does not allow us to strictly constrain the model parameters.

It is possible to stimate the WHIM covering factor from the ratio between the fluxes arising from the two component; from the best fit model we obtain in this way a covering factor of $0.50^{0.59}_{0.42}$. This is to be compared with the covering factor that can be evaluated from the net counts in the 0.3 – 2 keV band in the cross cone region with respect to the counts in the bicone region; assuming an inclination angle $i = 30^\circ$ (see Fischer et al. 2010) we obtain a covering factor of $0.60^{0.63}_{0.58}$, in agreement with the previous result.

7. CONCLUSIONS

We have presented results from new ACIS/*Chandra* observations of Seyfert 2 galaxy Mrk 573 obtained as part of CHEERS survey: these add to another existing observation performed in 2006 (PI: Bianchi) to reach an exposure time of ~ 110 ks, allowing us to study specific features of the soft X-ray emission (0.3 – 2 keV) from this source. In fact, soft X-ray emission from Seyfert galaxies shows a striking correspondence with NLR and ENLR as mapped by [O III] emission, suggesting an interplay between radio jets, optical and soft X-ray emission as shown by the comparison of the merged image of these observations with the *HST* and *VLA* images presented in Figure 2.

We have performed spectral analyses on different region of the source, and modeled the extracted spectra with different fitting models. In particular, the nuclear emission shows a slight decrease of the observed flux together with an increase in hydrogen column density, and is best fitted with a highly photoionized plasma; the cone emission, on the other hand, does not show significant flux variations, and is effectively modeled with a mildly photoionized plasma diffused over the bicone, with the contribution of a collisionally ionized phase at a temperature ~ 1 keV. This gas appears to be located in front of the observed radio knots, at the interface between the optical arcs and can be interpreted in terms of shock interaction of the radio ejecta with the galactic plane, with the jet depositing $\gtrsim 15\%$ of its power into the ISM.

These deep observations allow us to detect diffuse, soft X-ray emission extending up to ~ 13 kpc along the bicone axis, while in the region perpendicular to it, where the obscuring torus

is supposed to lie in the AGN unified model, we find significant emission extending up to $\sim 8''$ from the nucleus; this emission can be interpreted as nuclear continuum filtered by WHIM with a covering factor $\sim 50\%$, an ionization parameter ~ 1.3 and a hydrogen column density $\log N_H = 23.3$, somewhat in agreement with the unifying structure for the inner quasar regions presented by Elvis (2000). Deeper observations are however required in order to better constrain the model parameter in this region of faint emission.

We acknowledge useful comments and suggestions by our anonymous referee. This work is supported by NASA grant GO1-12009X and HST GO-12365.01-A (PI: Wang). We acknowledge support from the CXC, which is operated by the Smithsonian Astrophysical Observatory (SAO) for and on behalf of NASA under Contract NAS8-03060. A. P. thanks Andrea Marinucci, Francesco Massaro and Guido Risaliti for useful discussions. This research has made use of data obtained from the Chandra Data Archive, and software provided by the CXC in the application packages CIAO and Sherpa. Some of the data presented in this paper were obtained from the Multimission Archive at the Space Telescope Science Institute (MAST). STScI is operated by the Association of Universities for Research in Astronomy, Inc., under NASA contract NAS5-26555.

REFERENCES

- Antonucci, R. 1993, *ARA&A*, 31, 473
- Arnaud, K. A. 1996, *Astronomical Data Analysis Software and Systems V*, 101, 17
- Bianchi, S., Guainazzi, M., & Chiaberge, M. 2006, *A&A*, 448, 499
- Bianchi, S., Guainazzi, M., Matt, G., Fonseca Bonilla, N., & Ponti, G. 2009, *A&A*, 495, 421
- Bianchi, S., Chiaberge, M., Evans, D. A., et al. 2010, *MNRAS*, 405, 553
- Brinkman, A. C., Kaastra, J. S., van der Meer, R. L. J., et al. 2002, *A&A*, 396, 761
- Carter, C., Karovska, M., Jerius, D., Glotfelty, K., & Beikman, S. 2003, *Astronomical Data Analysis Software and Systems XII*, 295, 477
- Cavagnolo, K. W., McNamara, B. R., Nulsen, P. E. J., et al. 2010, *ApJ*, 720, 1066
- Condon, J. J., Yin, Q. F., Thuan, T. X., & Boller, T. 1998, *AJ*, 116, 2682
- Ebeling, H., White, D. A., & Rangarajan, F. V. N. 2006, *MNRAS*, 368, 65
- Elvis, M. 2000, *ApJ*, 545, 63

- Esch, D. N., Connors, A., Karovska, M., & van Dyk, D. A. 2004, *ApJ*, 610, 1213
- Falcke, H., Wilson, A. S., & Simpson, C. 1998, *ApJ*, 502, 199
- Ferland, G. J., Korista, K. T., Verner, D. A., et al. 1998, *PASP*, 110, 761
- Ferruit, P., Wilson, A. S., Falcke, H., et al. 1999, *MNRAS*, 309, 1
- Fischer, T. C., Crenshaw, D. M., Kraemer, S. B., Schmitt, H. R., & Trippe, M. L. 2010, *AJ*, 140, 577
- Fruscione, A., McDowell, J. C., Allen, G. E., et al. 2006, *Proc. SPIE*, 6270,
- Gonzalez-Martin, O., Acosta-Pulido, J. A., Perez Garcia, A. M., & Ramos Almeida, C. 2010, *ApJ*, 723, 1748
- Guainazzi, M., Matt, G., & Perola, G. C. 2005, *A&A*, 444, 119
- Guainazzi, M., & Bianchi, S. 2007, *MNRAS*, 374, 1290
- Hardcastle, M. J., Harris, D. E., Worrall, D. M., & Birkinshaw, M. 2004, *ApJ*, 612, 729
- Harris, D. E., Mossman, A. E., & Walker, R. C. 2004, *ApJ*, 615, 161
- Hollis, J. M., Lyon, R. G., Dorband, J. E., & Feibelman, W. A. 1997, *ApJ*, 475, 231
- Kalberla, P. M. W., Burton, W. B., Hartmann, D., et al. 2005, *A&A*, 440, 775
- Karovska, M., Schlegel, E., Hack, W., Raymond, J. C., & Wood, B. E. 2005, *ApJ*, 623, L137
- Karovska, M., Carilli, C. L., Raymond, J. C., & Mattei, J. A. 2007, *ApJ*, 661, 1048
- Kinkhabwala, A., Sako, M., Behar, E., et al. 2002, *ApJ*, 575, 732
- Komatsu, E., Smith, K. M., Dunkley, J., et al. 2011, *ApJS*, 192, 18
- Li, J., Kastner, J. H., Prigozhin, G. Y., & Schulz, N. S. 2003, *ApJ*, 590, 586
- Lucy, L. B. 1974, *AJ*, 79, 745
- Marinucci, A., Bianchi, S., Matt, G., et al. 2011, *A&A*, 526, A36
- Massaro, F., Bianchi, S., Matt, G., D’Onofrio, E., & Nicastro, F. 2006, *A&A*, 455, 153
- Mathur, S., Elvis, M., & Wilkes, B. 1995, *ApJ*, 452, 230
- Ogle, P. M., Marshall, H. L., Lee, J. C., & Canizares, C. R. 2000, *ApJ*, 545, L81

- Perlman, E. S., Padgett, C. A., Georganopoulos, M., et al. 2010, *ApJ*, 708, 171
- Porquet, D., & Dubau, J. 2000, *A&AS*, 143, 495
- Quillen, A. C., Alonso-Herrero, A., Rieke, M. J., et al. 1999, *ApJ*, 525, 685
- Raga, A. C., Noriega-Crespo, A., & Velázquez, P. F. 2002, *ApJ*, 576, L149
- Richardson, W. H. 1972, *Journal of the Optical Society of America* (1917-1983), 62, 55
- Risaliti, G., Elvis, M., & Nicastro, F. 2002, *ApJ*, 571, 234
- Ruiz, J. R., Crenshaw, D. M., Kraemer, S. B., et al. 2005, *AJ*, 129, 73
- Schlesinger, K., Pogge, R. W., Martini, P., Shields, J. C., & Fields, D. 2009, *ApJ*, 699, 857
- Schmitt, H. R., Donley, J. L., Antonucci, R. R. J., Hutchings, J. B., & Kinney, A. L. 2003, *ApJS*, 148, 327
- Siemiginowska, A., Stawarz, Ł., Cheung, C. C., et al. 2007, *ApJ*, 657, 145
- Ulvestad, J. S., & Wilson, A. S. 1984, *ApJ*, 278, 544
- Wang, J. 2010, *Chandra Proposal*, 3033
- Wang, J., Fabbiano, G., Risaliti, G., et al. 2011a, *ApJ*, 729, 75
- Wang, J., Fabbiano, G., Elvis, M., et al. 2011b, *ApJ*, 736, 62
- Wang, J., Fabbiano, G., Elvis, M., et al. 2011c, *ApJ*, 742, 23

A. Spectral fits results

In this Appendix we present results of spectral fits for the models presented in Sects. 4.1 and 4.2, both for the nuclear (Tables 3, 4 and Figures 13, 5) and the cone (Tables 5, 6 and Figures 15, 16) regions. When possible, fits were performed each observation as well as on merged observations.

Table 3: Measured line fluxes of the nuclear region

Obs. ID.		07745	12294	13124	13125	CHEERS OBS	ALL OBS
Net Counts (0.3 - 2 keV)		2109(46)	460(21)	2308(48)	765(28)	3533(59)	5642(75)
Line	Energy ^a	Flux ^b					
C V Hey	0.371	11.36 ^{17.02} _{10.19}	-	12.22 ^{14.47} _{9.91}	-	11.88 ^{13.99} _{9.76}	12.71 ^{13.26} _{12.18}
N VI triplet	0.426	-	-	-	-	-	-
C VI Ly β	0.436	5.83 ^{7.58} _{4.08}	7.57 ^{10.08} _{5.26}	2.80 ^{3.66} _{1.85}	4.21 ^{4.80} _{3.61}	2.87 ^{3.68} _{2.04}	3.65 ^{3.83} _{3.42}
N VII Ly α	0.500	5.21 ^{6.24} _{4.18}	0.96 ^{2.26} _{0.00}	2.29 ^{2.82} _{1.76}	5.34 ^{5.71} _{4.98}	2.67 ^{3.12} _{2.22}	3.28 ^{3.41} _{3.16}
O VII triplet	0.569	9.75 ^{10.77} _{8.73}	7.02 ^{8.71} _{5.64}	6.90 ^{7.51} _{6.29}	7.21 ^{7.58} _{6.84}	7.00 ^{7.50} _{6.50}	7.76 ^{7.89} _{7.63}
O VIII Ly α	0.654	3.13 ^{3.57} _{2.70}	1.74 ^{2.87} _{1.24}	1.56 ^{1.88} _{1.28}	2.49 ^{2.65} _{2.32}	1.79 ^{2.04} _{1.57}	2.14 ^{2.19} _{2.07}
O VII Hey	0.698	-	0.61 ^{1.08} _{0.07}	-	-	-	-
Fe XVII 3s2	0.727	-	-	0.21 ^{0.43} _{0.00}	-	-	-
O VII RRC	0.739	2.09 ^{2.43} _{1.75}	-	1.34 ^{1.77} _{1.13}	0.54 ^{0.65} _{0.43}	1.21 ^{1.38} _{0.99}	1.45 ^{1.48} _{1.39}
Fe XVII 3d2p	0.826	1.86 ^{2.22} _{1.36}	1.36 ^{1.75} _{0.85}	1.10 ^{1.27} _{0.90}	1.35 ^{1.44} _{1.25}	1.16 ^{1.35} _{1.02}	1.33 ^{1.37} _{1.30}
O VIII RRC	0.871	0.29 ^{1.02} _{0.00}	0.80 ^{1.28} _{0.37}	-	-	0.05 ^{0.19} _{0.00}	0.11 ^{0.12} _{0.05}
Ne IX triplet	0.915	2.24 ^{2.68} _{1.62}	1.08 ^{1.55} _{0.03}	1.61 ^{1.77} _{1.46}	1.50 ^{1.59} _{1.40}	1.58 ^{1.80} _{1.45}	1.75 ^{1.79} _{1.72}
Fe XX 3d2p	0.965	0.25 ^{0.60} _{0.00}	1.28 ^{1.84} _{0.94}	0.23 ^{0.37} _{0.12}	0.13 ^{0.20} _{0.04}	0.32 ^{0.43} _{0.13}	0.32 ^{0.34} _{0.29}
Ne X Ly α	1.022	1.10 ^{1.30} _{0.89}	0.08 ^{0.32} _{0.00}	0.35 ^{0.45} _{0.26}	0.82 ^{0.89} _{0.76}	0.39 ^{0.51} _{0.31}	0.55 ^{0.57} _{0.52}
Ne IX Hey	1.127	0.44 ^{0.56} _{0.33}	0.41 ^{0.63} _{0.20}	0.22 ^{0.32} _{0.14}	0.35 ^{0.40} _{0.30}	0.33 ^{0.45} _{0.26}	0.40 ^{0.42} _{0.38}
Ne IX He δ	1.152	-	-	0.31 ^{0.46} _{0.23}	-	0.15 ^{0.35} _{0.08}	0.07 ^{0.09} _{0.05}
Ne X Ly β	1.211	0.51 ^{0.62} _{0.40}	0.41 ^{0.59} _{0.31}	0.27 ^{0.34} _{0.19}	0.28 ^{0.32} _{0.24}	0.30 ^{0.39} _{0.24}	0.38 ^{0.39} _{0.36}
Mg XI triplet	1.352	0.53 ^{0.63} _{0.43}	0.59 ^{0.77} _{0.41}	0.49 ^{0.56} _{0.42}	0.23 ^{0.26} _{0.19}	0.44 ^{0.50} _{0.38}	0.47 ^{0.48} _{0.45}
Fe XXII 4p2p	1.425	0.16 ^{0.24} _{0.07}	0.18 ^{0.33} _{0.01}	0.08 ^{0.13} _{0.02}	-	0.06 ^{0.11} _{0.02}	0.09 ^{0.11} _{0.08}
Si XIII triplet	1.839	0.32 ^{0.40} _{0.25}	-	0.21 ^{0.26} _{0.16}	0.15 ^{0.19} _{0.12}	0.19 ^{0.23} _{0.15}	0.23 ^{0.24} _{0.22}
Power-Law norm.		3.68 ^{4.19} _{3.17}	4.48 ^{5.23} _{3.76}	4.20 ^{4.52} _{3.90}	4.72 ^{4.89} _{4.56}	4.28 ^{4.53} _{4.02}	4.06 ^{4.14} _{4.00}
χ^2 (dof)		0.92(50)	1.28(4)	1.28(55)	0.52(14)	1.21(102)	1.63(169)
$F_{(0.3-2)}$ ^c		5.27 ^{5.46} _{5.08}	3.69 ^{3.91} _{3.47}	4.01 ^{4.16} _{3.86}	3.75 ^{3.93} _{3.57}	4.05 ^{4.18} _{3.91}	4.37 ^{4.48} _{4.26}

Notes:

^a Line rest-frame energy in keV.

^b Line fluxes in units of 10^{-5} photons $\text{cm}^{-2} \text{s}^{-1}$.

^c Unabsorbed flux in the 0.3 – 2 keV band in units of 10^{-13} erg $\text{cm}^{-2} \text{s}^{-1}$.

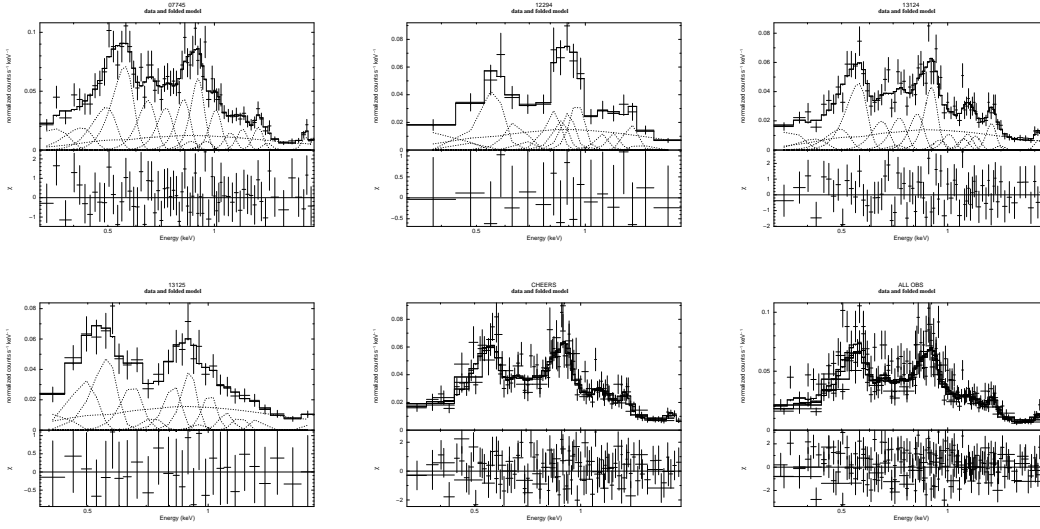


Fig. 13.— *Chandra* ACIS-S 0.3 – 2 keV spectra of the nuclear emission in different observations, with best fit emission lines models.

Table 4: Best fit photoionization models for the nuclear region

Obs. ID.	07745	12294	13124	13125	CHEERS OBS	ALL OBS
Net Counts (0.3 - 10 keV)	2352(48)		2663(52)		4063(64)	6415(80)
Model Parameter						
$\log(U_1)$	$1.09^{1.14}_{1.05}$	$1.12^{1.19}_{1.06}$	$1.04^{1.06}_{1.02}$	$1.16^{1.22}_{1.04}$	$1.06^{1.08}_{1.04}$	$1.08^{1.10}_{1.06}$
$\log(N_{H1})$	$20.47^{20.72}_{20.21}$	$21.72^{22.06}_{21.31}$	$20.89^{20.96}_{20.82}$	$20.92^{21.36}_{20.70}$	$20.94^{21.00}_{20.90}$	$20.90^{20.99}_{20.83}$
$F_{1(0.3-2)}^a$	$2.71^{2.93}_{2.50}$	$2.94^{3.18}_{2.08}$	$1.96^{2.06}_{1.87}$	$2.22^{2.52}_{1.97}$	$2.04^{2.13}_{1.98}$	$2.24^{2.36}_{2.14}$
$F_{1(2-10)}^a$	$0.38^{0.44}_{0.31}$	$0.68^{0.93}_{0.51}$	$0.31^{0.33}_{0.29}$	$0.39^{0.48}_{0.32}$	$0.32^{0.36}_{0.30}$	$0.35^{0.36}_{0.33}$
$\log(U_2)$	$-0.74^{-0.57}_{-0.91}$	$-0.84^{0.54}_{-1.05}$	$-0.73^{-0.70}_{-0.77}$	$-0.88^{-0.68}_{-0.99}$	$-0.71^{-0.58}_{-0.80}$	$-0.75^{-0.72}_{-0.79}$
$\log(N_{H2})$	$20.21^{20.58}_{19.86}$	$21.78^{22.57}_{20.98}$	$20.81^{20.87}_{20.74}$	$21.48^{21.93}_{20.02}$	$21.04^{21.35}_{20.77}$	$20.66^{20.73}_{20.60}$
$F_{2(0.3-2)}^a$	$2.79^{3.10}_{2.51}$	$0.93^{1.40}_{0.65}$	$1.48^{1.60}_{1.36}$	$2.17^{2.88}_{1.57}$	$1.53^{1.64}_{1.46}$	$1.88^{1.95}_{1.79}$
$F_{2(2-10)}^a$	$0.23^{0.30}_{0.17}$	$0.29^{0.35}_{0.11}$	$0.16^{0.17}_{0.14}$	$0.45^{1.15}_{0.21}$	$0.18^{0.20}_{0.14}$	$0.20^{0.21}_{0.19}$
kT^b	-	-	-	-	-	-
Refl ^c	$1.06^{1.30}_{0.84}$	$0.67^{1.00}_{0.26}$	$0.67^{0.81}_{0.54}$	$0.80^{1.18}_{0.46}$	$0.63^{0.79}_{0.53}$	$0.82^{0.94}_{0.73}$
$E_{SiK\alpha}^d$	1.839*	1.839*	1.839*	1.839*	1.839*	1.839*
$F_{SiK\alpha}^e$	$0.13^{0.19}_{0.06}$	< 0.08	$0.10^{0.15}_{0.05}$	$0.10^{0.20}_{0.00}$	$0.08^{0.12}_{0.04}$	$0.10^{0.14}_{0.06}$
$E_{SK\alpha}^d$	2.430*	2.430*	2.430*	2.430*	2.430*	2.430*
$F_{SK\alpha}^e$	$0.17^{0.25}_{0.09}$	< 0.38	$0.12^{0.18}_{0.07}$	< 0.20	$0.11^{0.16}_{0.06}$	$0.13^{0.17}_{0.09}$
$E_{FeK\alpha}^d$	$6.35^{6.37}_{6.34}$	-	$6.51^{6.61}_{6.47}$	$6.04^{7.38}_{5.83}$	$6.56^{6.66}_{6.52}$	$6.46^{6.54}_{6.42}$
$F_{FeK\alpha}^e$	$0.91^{1.08}_{0.73}$	-	$1.18^{1.38}_{1.00}$	$0.86^{1.29}_{0.60}$	$1.25^{1.40}_{0.91}$	$1.11^{1.27}_{0.95}$
$\chi^2(\text{dof})$	0.97(66)	0.83(13)	1.42(76)	1.17(23)	1.21(132)	1.55(211)
$F_{(0.3-2)}^a$	$5.76^{5.96}_{5.57}$	$4.02^{4.25}_{3.71}$	$4.03^{4.14}_{3.95}$	$4.41^{4.60}_{4.31}$	$4.08^{4.15}_{4.02}$	$4.53^{4.62}_{4.48}$
$F_{(2-10)}^a$	$3.74^{4.08}_{3.41}$	$2.26^{2.88}_{1.94}$	$3.64^{3.75}_{3.54}$	$3.30^{3.78}_{2.89}$	$3.37^{3.72}_{3.26}$	$3.76^{3.85}_{3.65}$

Notes:

^a Unabsorbed flux in units of 10^{-13} erg cm⁻² s⁻¹.

^b Plasma temperature in keV.

^c Normalization of the reflection component in units of 10^{-3} photons keV¹ cm⁻² s⁻¹

^d Line rest-frame energy in keV.

^e Line fluxes in units of 10^{-5} photons cm⁻² s⁻¹.

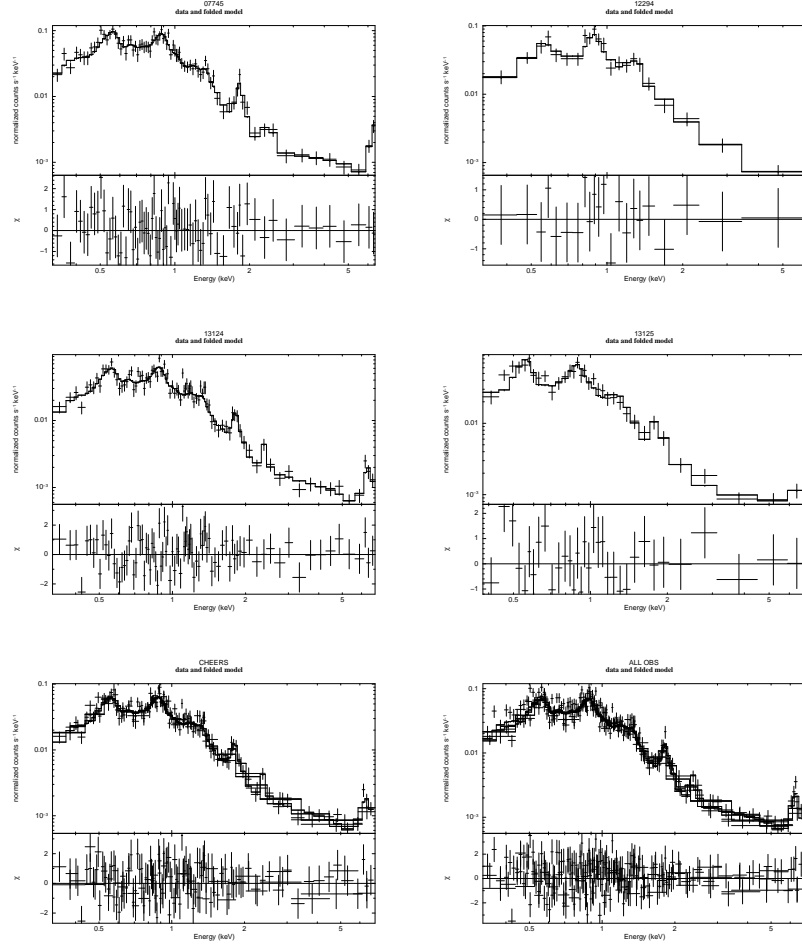


Fig. 14.— *Chandra* ACIS-S 0.3 – 10 keV spectra of the nuclear emission in different observations, with best fit photoionization models.

Table 5: Measured line fluxes of the cone regions

Obs. ID		07745		13124		CHEERS OBS		ALL OBS	
Cone		NW	SE	NW	SE	NW	SE	NW	SE
Net Counts (0.3 - 2 keV)		358(19)	277(17)	424(21)	371(19)	656(26)	550(24)	1013(32)	826(29)
Line	Energy ^a	Flux ^b							
C V Hey	0.371	-	-	-	-	-	-	-	-
N VI triplet	0.426	-	-	-	-	-	-	-	-
C VI Lyβ	0.436	1.00 ^{1.84} _{0.15}	1.29 ^{1.65} _{0.92}	0.87 ^{1.21} _{0.54}	1.85 ^{2.20} _{1.50}	0.82 ^{1.15} _{0.49}	1.76 ^{2.10} _{1.43}	0.83 ^{1.13} _{0.53}	1.56 ^{1.81} _{1.31}
N VII Lyα	0.500	0.57 ^{0.97} _{0.18}	-	0.19 ^{0.41} _{0.00}	-	0.17 ^{0.38} _{0.00}	-	0.29 ^{0.47} _{0.11}	-
O VII triplet	0.569	1.20 ^{1.32} _{0.88}	1.63 ^{1.89} _{1.37}	1.16 ^{1.41} _{0.91}	1.35 ^{1.56} _{1.14}	1.11 ^{1.35} _{0.87}	1.32 ^{1.51} _{1.13}	1.15 ^{1.33} _{0.96}	1.47 ^{1.60} _{1.29}
O VIII Lyα	0.654	0.35 ^{0.48} _{0.21}	0.33 ^{0.46} _{0.20}	0.40 ^{0.51} _{0.28}	0.41 ^{0.51} _{0.30}	0.37 ^{0.47} _{0.27}	0.42 ^{0.52} _{0.33}	0.36 ^{0.44} _{0.28}	0.39 ^{0.47} _{0.31}
O VII Hey	0.698	-	-	-	-	-	-	-	-
Fe XVII 3s2	0.727	-	-	-	-	-	-	-	-
O VII RRC	0.739	0.28 ^{0.40} _{0.17}	0.26 ^{0.36} _{0.16}	0.41 ^{0.51} _{0.32}	0.26 ^{0.34} _{0.18}	0.45 ^{0.53} _{0.36}	0.27 ^{0.34} _{0.20}	0.38 ^{0.45} _{0.31}	0.26 ^{0.32} _{0.21}
Fe XVII 3d2p	0.826	0.14 ^{0.31} _{0.00}	0.22 ^{0.29} _{0.14}	0.12 ^{0.25} _{0.09}	0.11 ^{0.16} _{0.05}	0.13 ^{0.24} _{0.01}	0.11 ^{0.16} _{0.06}	0.13 ^{0.23} _{0.03}	0.15 ^{0.19} _{0.11}
O VIII RRC	0.871	0.30 ^{0.32} _{0.09}	-	0.09 ^{0.25} _{0.00}	-	0.11 ^{0.26} _{0.00}	-	0.16 ^{0.30} _{0.04}	-
Ne IX triplet	0.915	0.20 ^{0.32} _{0.08}	0.15 ^{0.21} _{0.10}	0.16 ^{0.24} _{0.07}	0.20 ^{0.25} _{0.16}	0.16 ^{0.24} _{0.08}	0.20 ^{0.24} _{0.16}	0.17 ^{0.24} _{0.10}	0.18 ^{0.22} _{0.15}
Fe XX 3d2p	0.965	-	-	-	-	-	-	-	-
Ne X Lyα	1.022	0.12 ^{0.16} _{0.07}	0.05 ^{0.08} _{0.02}	0.11 ^{0.14} _{0.07}	0.09 ^{0.12} _{0.06}	0.11 ^{0.15} _{0.08}	0.09 ^{0.11} _{0.06}	0.11 ^{0.14} _{0.09}	0.08 ^{0.10} _{0.06}
Ne IX Hey	1.127	0.10 ^{0.13} _{0.06}	-	-	-	-	-	-	-
Ne IX Heδ	1.152	-	-	0.03 ^{0.06} _{0.00}	-	0.04 ^{0.07} _{0.01}	0.02 ^{0.03} _{0.00}	0.06 ^{0.08} _{0.04}	0.01 ^{0.03} _{0.00}
Ne X Lyβ	1.211	-	-	-	-	-	-	-	-
Mg XI triplet	1.352	0.05 ^{0.11} _{0.00}	-	0.03 ^{0.05} _{0.00}	0.04 ^{0.06} _{0.02}	0.02 ^{0.05} _{0.00}	0.04 ^{0.06} _{0.02}	0.02 ^{0.05} _{0.00}	0.03 ^{0.05} _{0.02}
Fe XXII 4p2p	1.425	-	-	-	-	-	-	-	-
Si XIII triplet	1.839	-	-	-	-	-	-	-	-
Power-Law norm.		0.39 ^{0.58} _{0.19}	0.35 ^{0.43} _{0.27}	0.43 ^{0.52} _{0.34}	0.30 ^{0.36} _{0.25}	0.43 ^{0.52} _{0.34}	0.27 ^{0.33} _{0.21}	0.43 ^{0.50} _{0.35}	0.27 ^{0.34} _{0.21}
χ ² (dof)		0.21(3)	1.13(3)	0.68(6)	0.39(7)	0.69(15)	0.26(13)	0.88(30)	0.53(24)
F _{0.3-2} ^c		0.53 ^{0.58} _{0.48}	0.45 ^{0.49} _{0.42}	0.47 ^{0.50} _{0.44}	0.46 ^{0.49} _{0.44}	0.46 ^{0.49} _{0.44}	0.45 ^{0.48} _{0.43}	0.48 ^{0.50} _{0.46}	0.45 ^{0.47} _{0.43}

Notes:

^a Line rest-frame energy in keV.

^b Line fluxes in units of 10⁻⁵ photons cm⁻² s⁻¹.

^c Unabsorbed flux in the 0.3 – 2 keV band in units of 10⁻¹³ erg cm⁻² s⁻¹.

Table 6: Best fit photoionization models for the cone regions

Obs. ID	07745		13124		CHEERS OBS		ALL OBS	
	NW	SE	NW	SE	NW	SE	NW	SE
log(<i>U</i> ₁)	0.25 ^{0.43} _{0.07}	0.28 ^{0.37} _{0.19}	0.27 ^{0.38} _{0.16}	0.50 ^{0.83} _{0.34}	0.29 ^{0.41} _{0.17}	0.50 ^{0.65} _{0.28}	0.27 ^{0.35} _{0.19}	0.47 ^{0.62} _{0.26}
log(<i>N</i> _{H1})	20.63 ^{21.71} _{19.55}	20.14 ^{20.71} _{19.58}	20.42 ^{21.10} _{19.73}	21.08 ^{21.89} _{20.27}	20.20 ^{20.87} _{19.54}	20.52 ^{21.39} _{19.65}	20.47 ^{20.89} _{19.91}	20.67 ^{21.58} _{19.76}
<i>F</i> _{1(0.3–2)} ^a	0.35 ^{0.38} _{0.34}	0.47 ^{0.38} _{0.04}	0.37 ^{0.44} _{0.31}	0.23 ^{0.33} _{0.09}	0.36 ^{0.44} _{0.24}	0.24 ^{0.35} _{0.14}	0.36 ^{0.41} _{0.30}	0.19 ^{0.27} _{0.11}
log(<i>U</i> ₂)	-2*	-1*	-2*	-1*	-2*	-1*	-2*	-1*
log(<i>N</i> _{H2})	20*	20*	20*	20*	20*	20*	20*	20*
<i>F</i> _{2(0.3–2)} ^a	0.28 ^{0.41} _{0.13}	≤ 0.03	0.12 ^{0.23} _{0.06}	0.28 ^{0.41} _{0.18}	0.11 ^{0.22} _{0.06}	0.27 ^{0.37} _{0.17}	0.14 ^{0.21} _{0.04}	0.32 ^{0.39} _{0.24}
<i>kT</i> ^b	0.84 ^{0.94} _{0.74}	-	0.78 ^{0.88} _{0.69}	1.02 ^{1.17} _{0.85}	0.75 ^{0.83} _{0.66}	0.99 ^{1.14} _{0.83}	0.77 ^{0.83} _{0.72}	0.84 ^{0.98} _{0.75}
<i>F</i> _{C(0.3–2)} ^a	0.10 ^{0.14} _{0.07}	-	0.08 ^{0.12} _{0.06}	0.03 ^{0.07} _{0.02}	0.09 ^{0.15} _{0.07}	0.04 ^{0.09} _{0.02}	0.10 ^{0.13} _{0.08}	0.05 ^{0.05} _{0.03}
χ ² (dof)	0.84(9)	1.33(7)	1.26(12)	0.44(10)	1.10(21)	0.36(17)	1.07(36)	0.58(28)
<i>F</i> _{0.3–2} ^a	0.74 ^{0.84} _{0.63}	0.50 ^{0.62} _{0.46}	0.57 ^{0.64} _{0.52}	0.56 ^{0.61} _{0.52}	0.56 ^{0.61} _{0.52}	0.56 ^{0.61} _{0.52}	0.60 ^{0.64} _{0.55}	0.56 ^{0.59} _{0.52}

Notes:

^a Unabsorbed flux in the 0.3 – 2 keV band in units of 10⁻¹³ erg cm⁻² s⁻¹.

^b Plasma temperature in keV.

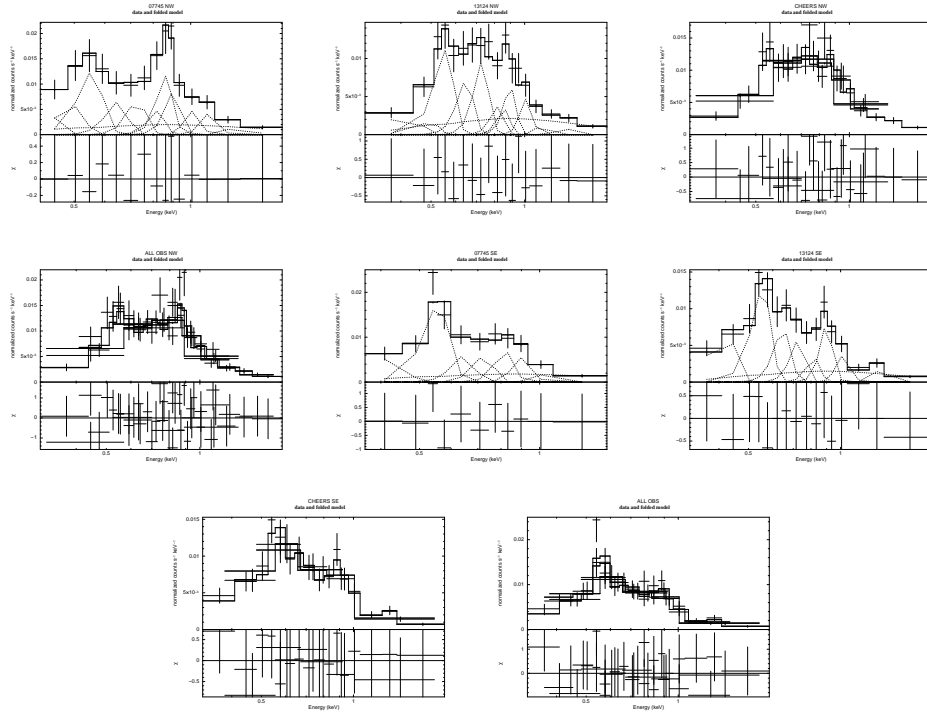


Fig. 15.— *Chandra* ACIS-S 0.3 – 2 keV spectra of the NW (top) and SE (bottom) cone emission in different observations, with best fit emission lines models.

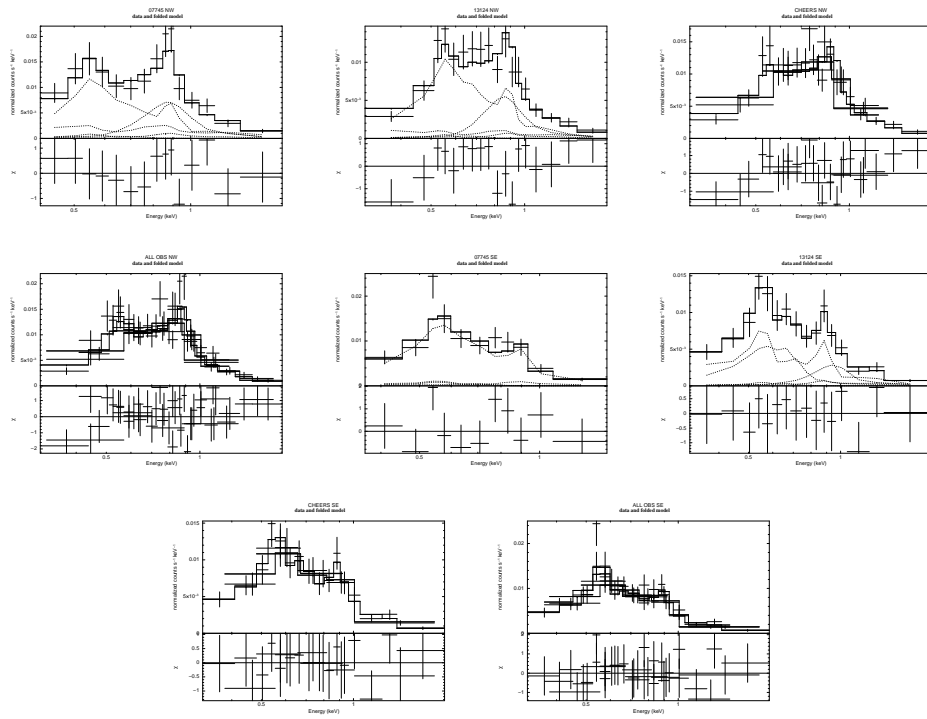


Fig. 16.— *Chandra* ACIS-S 0.3 – 2 keV spectra of the NW (top) and SE (bottom) cone emission in different observations, with best fit photoionization models.